ARTICLES
https://doi.org/10.1038/s41551-019-0393-4
nature biomedical engineering

Spectral tracing of deuterium for imaging glucose metabolism

Luyuan Zhang[1,3], Lingyan Shi[1,3], Yihui Shen[1,3], Yupeng Miao[1], Mian Wei[1], Naixin Qian[1], Yinong Liu[1] and Wei Min[1,2*]

Cells and tissues often display pronounced spatial and dynamical metabolic heterogeneity. Common glucose-imaging techniques report glucose uptake or catabolism activity, yet do not trace the functional utilization of glucose-derived anabolic products. Here we report a microscopy technique for the optical imaging, via the spectral tracing of deuterium (STRIDE), of diverse macromolecules derived from glucose. Based on stimulated Raman-scattering imaging, STRIDE visualizes the metabolic dynamics of newly synthesized macromolecules, such as DNA, protein, lipids and glycogen, via the enrichment and distinct spectra of carbon–deuterium bonds transferred from the deuterated glucose precursor. STRIDE can also use spectral differences derived from different glucose isotopologues to visualize temporally separated glucose populations using a pulse–chase protocol. We also show that STRIDE can be used to image glucose metabolism in many mouse tissues, including tumours, brain, intestine and liver, at a detection limit of 10 mM of carbon–deuterium bonds. STRIDE provides a high-resolution and chemically informative assessment of glucose anabolic utilization.

Glucose is arguably the most essential nutrient for animals. It supplies central metabolism, and is therefore of pivotal importance for the sustenance of cellular homoeostasis and growth. Glucose metabolism can be regulated by various cell-dependent and tissue-dependent factors, such as energy expenditure, biosynthesis demand and nutrient accessibility[1–3]. Hence, metabolic heterogeneity is prominent across different scales, such as in hierarchically organized tissues[4,5] and metabolically reprogrammed tumours[2]. Consequently, a number of powerful glucose-imaging tools have been developed for fundamental studies as well as for diagnostics. Positron emission tomography reports glucose uptake activity using [^{18}F]-fluorodeoxyglucose, a non-metabolizable glucose analogue[6]. NMR-based imaging measures glucose accumulation via saturation transfer from hydroxyl protons to water[7]. ^{13}C NMR spectroscopic imaging resolves soluble glycolytic products via hyperpolarized [^{13}C]-glucose[8]. Imaging mass spectrometry with isotope-labelled glucose provides chemical analysis of metabolites or their ion fragments desorbed from the sample with certain mass coverage[9,10]. Optical imaging can provide an in situ approach with high resolution. In particular, fluorescence or Raman imaging can report glucose uptake activity using non-metabolizable glucose analogues[11,12].

Glucose metabolism consists of multifaceted processes spanning from catabolism to anabolism and macromolecule synthesis[13]. Specifically, after being taken up into the cell, glucose catabolism breaks down carbon chains for the supply of energy, meanwhile providing substrate for biosynthesis of a variety of precursors including nucleotides, amino acids and fatty acids. These anabolic products further feed cell renewal and proliferation by building biological macromolecules. Excess glucose can also be stored as polymers (for example, glycogen in animals). It has been increasingly recognized that the diverging allocation of glucose towards synthesis of various macromolecules (such as nucleic acids, glycogen, protein and lipids) is an important manifestation of cells' functional status. Notable examples include reprogramming of glucose metabolism dedicated to biomass production for tumour cell proliferation[14,15] and the intricate crosstalk of metabolic regulation between glucose and lipid in liver[16,17]. However, the existing glucose-imaging tools mentioned above (such as PET, NMR and fluorescence) are mostly designed for visualizing the earlier processes of glucose metabolism including uptake or flux into small-molecule metabolites. The later utilization of glucose anabolic products towards macromolecule synthesis remains largely inaccessible to these imaging techniques. Hence, a technical advance in this area would not only help to provide a fuller picture of glucose metabolism but would also convey valuable information about the functional status of cells, tissues and organs.

Raman spectroscopy characterizes molecular vibrations by their inelastic photon scattering, and thus provides information on the concentration and composition of chemical bonds inside a specimen. Different types of molecules can be identified on the basis of their signature chemical moieties, such as CH_2 for lipid and amide or CH_3 for protein. However, Raman (micro)spectroscopy relies on weak spontaneous scattering, and is therefore not ideal for high-speed imaging. Detection, sensitivity and imaging speed are greatly improved in stimulated Raman scattering (SRS) microscopy[18–21]. As a nonlinear optical technique, SRS uses two synchronized pulsed lasers (usually in the near infrared or visible range), which create a beating field at their difference frequency to selectively accelerate the matching molecular vibrational transition by up to 10^8 times. The resulting intensity change of the incident beams (denoted as stimulated Raman loss or gain) after light–molecule interaction is proportional to the analyte concentration, whereas the quadratic laser power dependence enables three-dimensional optical sectioning. SRS fully preserves the spectra of spontaneous Raman scattering. A stack of hyperspectral images (at selected frequencies) can therefore be obtained by tuning the laser wavelength. In this manner, non-vibrational-resonance background can be subtracted by acquiring images at off-peak frequency. The spatial resolution and tissue penetration are similar to those in two-photon fluorescence microscopy, and are suitable for high-resolution imaging of animal tissues.

[1]Department of Chemistry, Columbia University, New York, NY, USA. [2]Kavli Institute for Brain Science, Columbia University, New York, NY, USA.
[3]These authors contributed equally: Luyuan Zhang, Lingyan Shi, Yihui Shen. *e-mail: wm2256@columbia.edu

Here, towards this unmet goal of mapping glucose metabolism, we develop spectral tracing of deuterium isotope (STRIDE) microscopy for high-spatial-resolution mapping of glucose-derived macromolecule synthesis activity, based on Raman spectroscopy and SRS imaging. We administered deuterium-labelled glucose ([D]-glucose) to cells or mice, and tracked the enrichment of carbon–deuterium (C–D) bonds in macromolecules with multichannel SRS microscopy. C–D bonds produce distinct Raman peaks in a 'cell-silent' window without interference from endogenous molecules, which reports metabolic activity[21–23]. For chemical specificity, we utilized C–D Raman spectral signatures that distinguish various types of glucose-derived macromolecules, which we attributed to the chemical environment experienced by the C–D bond in the macromolecules. This principle of STRIDE, together with a linear unmixing algorithm that we developed, enables visualization and interpretation of how glucose is allocated to diverging biosynthesis pathways for protein, lipid, nucleic acids and glycogen. We coupled STRIDE with multichannel SRS imaging to dissect multiple macromolecule biosynthesis pathways in vivo. In cases where C–D bond enrichment was detectable by SRS (10 mM C–D bonds), we obtained tissue metabolic histology, through which we identified markedly high lipid synthesis activity in specific brain regions during development and surprisingly efficient lipid absorbing ability of the neonatal intestinal epithelium. We also assessed glucose utilization in tumour xenografts. Furthermore, we developed a two-colour pulse–chase technique by employing spectral fingerprinting derived from different glucose isotopologues and demonstrated visualization of biosynthetic activity in different time windows.

Results

[D_7]-glucose as a probe of macromolecule synthesis. We first validated that [D_7]-glucose, a glucose isotopologue with deuterium labelling on all its carbons, could be used as a metabolic probe of macromolecule synthesis for SRS microscopy. Raman spectra obtained from cells cultured in [D_7]-glucose-substituted medium revealed a band around 2,150 cm^{-1} in the cell-silent region (1,800–2,600 cm^{-1}), confirming the formation of C–D bonds in cells (Fig. 1a). We then acquired SRS images targeting at this frequency, the intensity of which is proportional to the concentration of C–D bonds and shows increments for up to 3 d (Fig. 1b). This rate is much slower than the reported glucose uptake rate (reaching steady state in an hour)[12], thereby reflecting long-term accumulation of C–D bonds derived from [D_7]-glucose. Indeed, signal from transported [D_7]-glucose can hardly be detected at our detection limit (~4 mM) (Fig. 1b and Supplementary Fig. 1a). Moreover, unlike a previously developed glucose-uptake reporter[12], the accumulated C–D signal is not affected by making the cell membrane permeable via fixation (in which case the small-molecule metabolites from glucose would have been depleted) (Supplementary Fig. 1b), yet it was reduced by inhibition of fatty acid synthesis (Supplementary Fig. 1c). Together, these measurements confirmed that the observed signal originated from newly accumulated macromolecules rather than small-molecule metabolites of [D_7]-glucose.

Compared with labelling in vitro cell cultures as demonstrated previously[24–26], it is much more difficult to predict glucose utilization in whole animals in vivo in the presence of many other nutrient sources. Towards this challenging goal, we investigated different in vivo administration approaches. We found administration of up to 10% [D_7]-glucose in drinking water to be a convenient non-invasive approach for metabolic labelling in mice[27]. After 10 d of labelling, post mortem tissue slices were obtained for SRS imaging through laser scanning (Fig. 1c). At the same frequency (2,150 cm^{-1}), C–D bond accumulation was successfully visualized in tissues such as muscle and fat pad, indicating broad appearance of metabolic activity (Fig. 1d). Non-resonance background was measured at 1,900 cm^{-1} by tuning the laser, and then subtracted from the on-resonance image (2,150 cm^{-1}). Using [D_7]-glucose or unlabelled glucose or an equal mixture of both, we were able to vary the deuterium fraction without changing the total glucose amount in drinking water. In these three conditions, average tissue SRS signal at 2,150 cm^{-1} is roughly proportional to the percentage of [D]-glucose in the drinking water, demonstrating highly specific and quantitative detection of C–D bonds by SRS imaging (Fig. 1e). This labelling and imaging procedure is for general application, and it can be optimized for specific cases. For example, the concentration of [D_7]-glucose can be lowered to 2% while still generating sufficient signal in the fat pad (Supplementary Fig. 1d). Live imaging is also possible in principle, leveraging the optical sectioning, good tissue penetration and in vivo compatibility of SRS microscopy[21]. Here we demonstrated live imaging of the mouse ear at a rate of 1.6 s per frame, from which flow of blood cells is evident in both on-resonance (2,150 cm^{-1}) and off-resonance (1,900 cm^{-1}) images (Fig. 1f and Supplementary Video 1).

Principle of STRIDE. Images acquired at a single frequency (2,150 cm^{-1}) map the overall accumulation of glucose-derived C–D bonds. Yet, as a universal carbon source, glucose should supply synthesis of diverse biomass including glycogen, nucleic acids, lipids and proteins. Such divergence is reflected in atom tracing of deuterium along the central metabolic pathways, showing deuterium labelling in various metabolic precursors[13] (Fig. 2a). Hence, C–D SRS signal should represent the mixed contribution from these macromolecules. Indeed, although methanol removed all the lipids (confirmed by SRS imaging targeting carbon–hydrogen bonds, which showed almost completely diminished signal in the lipid image but no change in the protein image), it cannot remove all the C–D signal in cells (Fig. 2b). How is the supplied glucose allocated for different macromolecule synthesis? The ability to address this question would not only provide a full picture of glucose metabolism, but also convey valuable information about functional status of cells, tissues and organs.

To distinguish the different macromolecules derived from [D_7]-glucose, we sought to identify underlying C–D Raman spectral signatures that are sensitive to chemical environment. Like NMR spectroscopy, in which nuclei can be distinguished by their local chemical environment[7,14], vibrational frequency in Raman spectra also reflects the local chemical environment of the bond, such as polarity. We postulated that chemically diverse macromolecules might create different C–D vibrational spectra. To test this, we first labelled cultured HeLa cells with [D_7]-glucose, from which we isolated lipids, proteins and nucleic acids. We then acquired and studied their Raman spectra. We also obtained Raman spectra from glycogen acutely accumulated in [D_7]-glucose-labelled mouse liver (verified by perchloric acid dissolvability; Supplementary Fig. 2a–c). Notably, though they span almost the same frequency range, C–D Raman spectra from the above four types of molecules exhibited remarkably different peak positions and shapes from each other and from [D_7]-glucose solution (Fig. 2c) (peak frequency is summarized in Supplementary Table 1). Glycogen and nucleic acid, derived from glucose and (deoxy)ribose, show spectral features with multiple peaks (2,124, 2,170 and 2,234 cm^{-1}; Fig. 2c), corresponding to preservation of more C–D bonds as well as the distinct chemical environment attached to the sugar rings[28] (Fig. 2b). By contrast, protein and lipid, made from amino acids and fatty acids, respectively, show only one major peak (Fig. 2c). This is consistent with more loss of the deuterium going through glycolysis and the tricarboxylic acid cycle (Fig. 2b). To confirm this finding, we compared the results to the reference spectra of [D]-labelled fatty acids and amino acids (Supplementary Fig. 2d–f and Supplementary Table 1). We found good agreement between the peak frequency of the lipid extract (2,142 cm^{-1}) and singly labelled C–D in deuterated fatty acid (2,142 cm^{-1}), which is in a nonpolar aliphatic chemical environment.

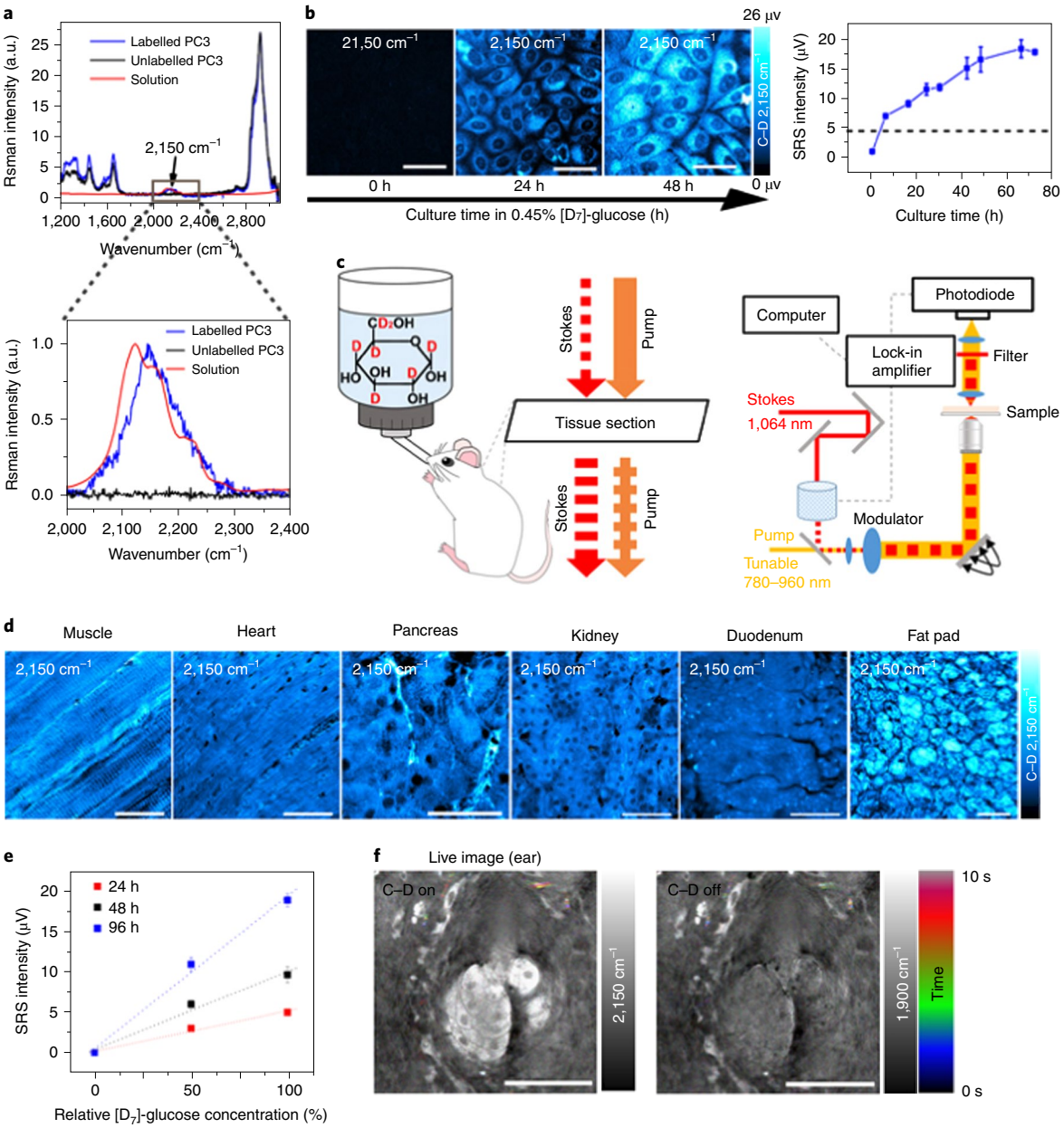

Fig. 1 | SRS imaging of overall metabolic activity by [D_7]-glucose labelling. a, Raman spectra normalized to C–D peak intensity, showing [D_7]-glucose solution (red), non-labelled PC3 cell (black) and PC3 cell labelled with 0.45% [D_7]-glucose for 72 h (blue). The boxed area corresponding to the cell-silent region is shown in the bottom graph. **b**, SRS imaging (at 2,150 cm^{-1}) of C–D label incorporation in PC3 cells labelled with 0.45% [D_7]-glucose for 0, 24 and 48 h. Time-dependent SRS intensity is quantified from the images (right). The dashed line indicates estimated signal from intracellular glucose (~10 mM; ref. [12]). Data are mean ± s.e.m.; $n = 30$. **c**, Experimental procedure. Mice were given [D_7]-glucose in drinking water. Post mortem tissue was sectioned and imaged by SRS microscopy using tunable near-infrared pulsed lasers and laser-scanning microscopy. A high-frequency modulation transfer scheme was used to extract SRS signal from transmitted light. **d**, SRS imaging (at 2,150 cm^{-1}) of C–D label incorporation in several tissues from a mouse (P30) after drinking 10% [D_7]-glucose or water for 10 d. **e**, SRS intensity quantified from mouse ear after labelling with 10% glucose, of which 0,50 or 100% was [D_7]-glucose, and the rest was unlabelled glucose. Three labelling durations (24, 48 and 96 h) were tested. Data are mean ± s.e.m.; $n = 4$. **f**, SRS images of ear skin from a living mouse that has been administered 5% [D_7]-glucose in drinking water for 8 d, showing temporal colour-coded on-resonance signal (2,150 cm^{-1}) and off-resonance background (1,900 cm^{-1}) channels acquired at 1.6 s per frame. Scale bars, 50 μm.

Similarly, the peak frequency of our protein extract (2,192 cm^{-1}) matches that from singly labelled C–D in deuterated amino acids (2,192 cm^{-1}), which is in a more polar chemical environment. These Raman spectral features reflect the distinct chemical environment experienced by C–D bonds in the specific biomacromolecules.

To further ensure that the Raman spectrum of each macromolecule discovered above is reproducible and accurate, we obtained in situ lipid and protein Raman spectra from [D_7]-glucose-labelled cells and mouse tissues by measuring signals that were susceptible and resistant to methanol washes, respectively (Supplementary Fig. 2g–j), and the Raman spectra from [D_7]-glucose-labelled tissue extracts (Supplementary Fig. 2k–l). All these spectra agree well with those from cell extracts. To improve accuracy, we then used the average of these spectra as our a priori standards to guide linear unmixing. We call this spectra-guided metabolic tracing technique STRIDE.

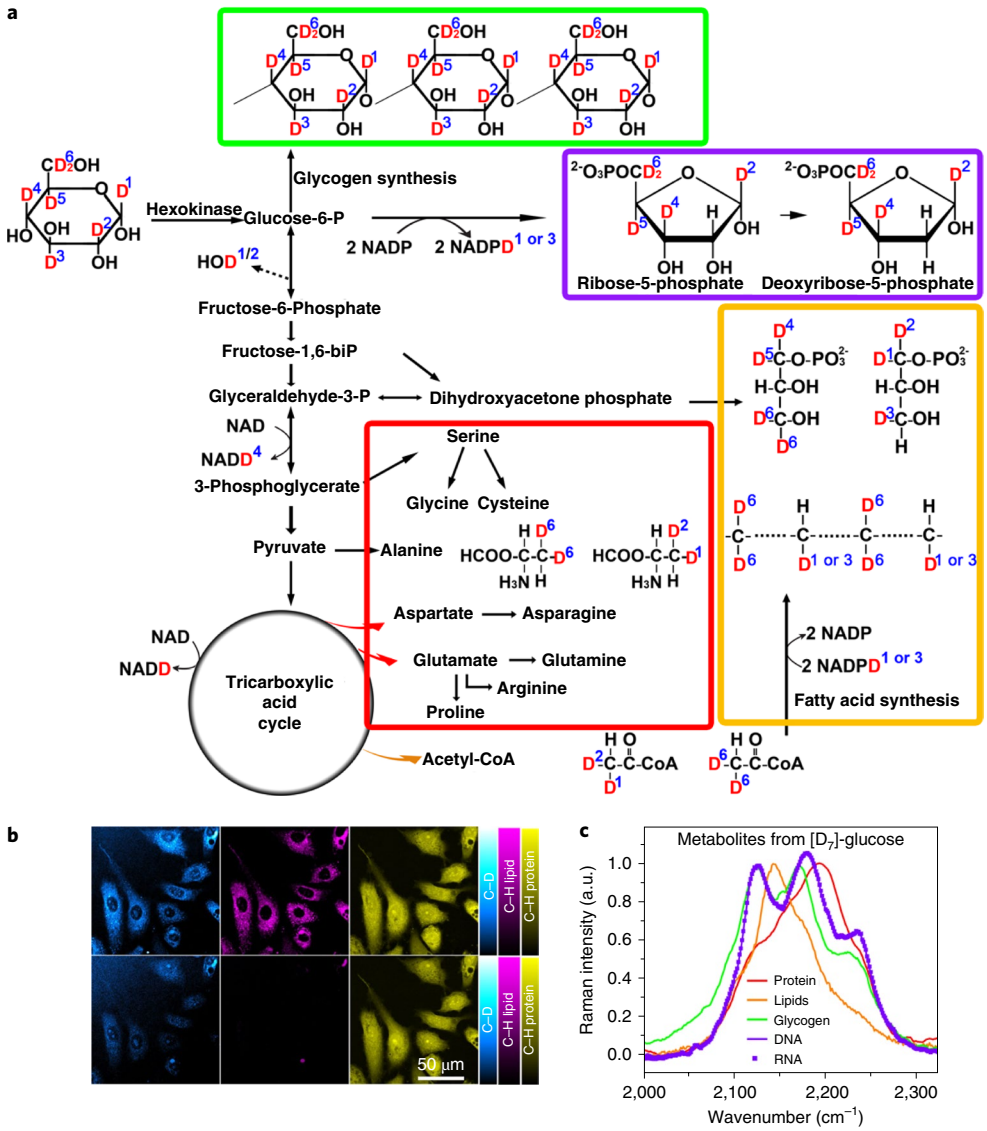

Fig. 2 | Principle of STRIDE. a, Deuterium transfer traced along major biosynthetic pathways derived from [D_7]-glucose. **b**, PC3 cells labelled with 0.45% [D_7]-glucose for 48 h, before (top) and after (bottom) methanol wash for 10 min. Images are also shown for unlabelled lipid (magenta) and protein (yellow) channel in the C–H frequencies. **c**, Normalized C–D Raman spectra of five glucose-derived macromolecule metabolites, including glycogen from [D_7]-glucose-fed mouse liver (fasted overnight and acutely stimulated and labelled by 10% [D_7]-glucose for 8 h), and protein, lipids, DNA and RNA extracted from HeLa cells cultured with 0.45% [D_7]-glucose for 6 d.

Multiplexed imaging of macromolecule synthesis with STRIDE. Next, we integrated STRIDE with multichannel SRS imaging. For *n* species with distinguishable spectra, linear unmixing can be performed with intensities at as few as *n* different frequencies (that is, channels). Therefore, we took SRS images at several selected frequencies by tuning the laser wavelength, and used the coefficients developed from the normalized standard spectra to calculate the unmixed images (Fig. 3). Here we leveraged the linear intensity–concentration dependence of SRS and the faithful correspondence of SRS intensity to that of Raman spectra[19]. We applied multichannel imaging and unmixing to HeLa cells cultured with [D_7]-glucose, where signals from de novo lipid synthesis (CD_L), protein synthesis (CD_P) and DNA replication (CD_D) are comparable to each other and can be successfully separated (Fig. 3a–c). Glycogen signal can be omitted in such non-specialized cell culture. DNA synthesis was detectable in mitotic cells with condensed chromosomes but not in non-mitotic cells due to the volume dilution (factor of 5; Supplementary Information and Supplementary Fig. 3a). It is therefore reasonable to omit DNA signal in non-mitotic cells in the remainder of this study. We also applied this technique to the liver of mice fed with [D_7]-glucose for 10 d and then acutely stimulated and labelled for 8 h after overnight fasting. With such labelling, signals from acute glycogen synthesis (CD_G) are comparable with CD_P and CD_L, and can be successfully separated (Fig. 3d–f). Distinct spatial patterns can be found in these channels. For example, CD_L signal reveals accumulation of lipid metabolites in lipid droplets, whereas CD_G reveals glycogen accumulation in cytoplasm, which shows as a halo pattern around the nucleus.

In addition to spatial information, quantitative information can be obtained by at least three means. First, absolute SRS intensity can be used to compare metabolic activity under different conditions. For example, we found that 16 h pre-starvation increased liver glycogen signal (Supplementary Fig. 3b). Second, the ratio between two macromolecule channels, such as CD_P and CD_L, can be used to indicate differential utilization of glucose metabolism. For example, we generated CD_P/CD_L ratio images for a variety of

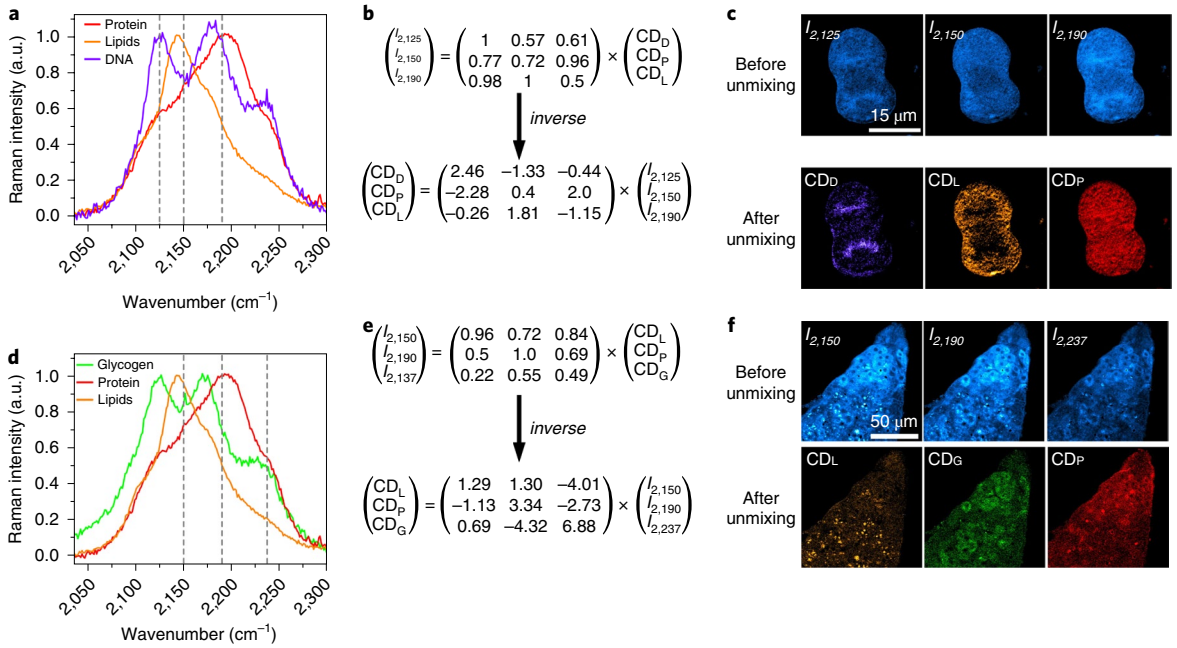

Fig. 3 | Multiplexed imaging of macromolecule biosynthesis activity using STRIDE of [D_7]-glucose. a, Raman spectra of [D_7]-glucose-derived proteins, lipids and DNA, as in Fig. 2c. Dashed lines indicate imaging frequencies for corresponding macromolecules. **b**, Linear unmixing algorithm for proteins, lipids and DNA. I_X, image intensity for corresponding frequencies. CD_X, calculated intensity for corresponding macromolecules. **c**, Images of a [D_7]-glucose-labelled mitotic HeLa cell before and after unmixing. **e**, Raman spectra of [D_7]-glucose-derived proteins, lipids and glycogen, as in Fig. 2c. Dashed lines indicate imaging frequencies for corresponding macromolecules. **f**, Linear unmixing algorithm for proteins, lipids, and glycogen. **g**, Images of a [D_7]-glucose-fed mouse liver before and after unmixing.

tissues, including heart, pancreas, kidney, duodenum, stomach and fat pad, thereby generating a tissue atlas of macromolecule-specific glucose metabolism (Fig. 4a). These ratio images captured highly specialized organs, such as cardiac muscle (high protein synthesis) and fat tissue (lipid synthesis) consistent with their metabolic functions. Notably, metabolic heterogeneity can also be observed at subcellular scale. For tissues along the gastrointestinal tract, the highest ratio (that is, predominantly protein synthesis) is generally found in nucleus, whereas the supportive tissue or duct has the lowest ratio (predominantly lipid synthesis).

The third method for quantitative interpretation uses the ratio of the C–D and C–H channels. SRS images targeted at the frequency of C–H (lipid, CH_L; protein, CH_P) map the concentration of unlabelled C–H bonds in lipid or protein[29]. Thus, intensity ratio between corresponding C–D and C–H channels reflects the renewal or turnover of the specific biomolecule. For example, we tracked the skin sebaceous gland of mice drinking 5% [D_7]-glucose water each day from days one to six. The lipid production and secretion in the sebaceous gland are known to use the holocrine mechanism, in which peripheral sebocytes rupture and release their contents in the central duct[30]. By calculating the CD_L/CH_L ratio image, we found that glucose-supplied lipid renewal actually first appeared on the periphery of gland and then gradually migrated to the centre (Fig. 4b). This offers an insight into the metabolic aspect of the holocrine secretion process. Moreover, with sufficient spatial resolution, remnants of sebocytes with much lower metabolic turnover could readily be found in the duct (for example, on day six).

This third quantification method using the CD/CH ratio also offers a checkpoint that can be cross-referenced with proton-NMR spectroscopy. We obtained hydrogen and deuterium NMR spectra of tissue lipid extracts and quantified the D/H ratio (Supplementary Fig. 4a). We also calculated the CD/CH ratio for both Raman spectra (using peak intensity) and SRS imaging (using area-averaged intensity). The ratios show good correspondence among the three different measurements (Supplementary Fig. 4b), validating the quantitative reliability of STRIDE.

STRIDE imaging of metabolic activity. With the three quantification methods introduced above, STRIDE imaging can be applied to study metabolic dynamics during development and in tumour progression. We labelled a young mouse during the developmental period (embryonic day (E)11 to postnatal day (P)21) by administering [D_7]-glucose in the drinking water (2%) to the mother, and mapped macromolecule synthesis in the tissues. We compared the brain of the young mouse (labelled during E11–P21) with that of an adult mouse labelled with the same concentration of [D_7]-glucose for the same duration. Whole-brain tissue mapping, as in SRS intensity, readily revealed faster basal-level lipid and protein metabolism in the young mouse brain compared with the adult brain (Fig. 5a). Quantitative comparison of the absolute SRS image intensity revealed highly active lipid synthesis in the young brain in comparison with the adult brain in multiple regions including caudoputamen (CP), fimbria (FI), optic tract (OPT), lateral habenula (LH), lateral hypothalamic area (HY), mammilothalmic tract (MTT), hippocampus (HPF), stria terminalis (ST) and corpus callosum (CC) in cerebrum (Fig. 5b and Supplementary Fig. 5a,b).

Comparing lipid signal between the CD and CH channels reveals a large age difference in lipid turnover, especially in the white matter of cerebellum (Fig. 5c). Intensity profiles across the cerebellum layers show active lipid turnover in the young brain but almost no turnover in the adult brain (Fig. 5d). The patterns in young brain are spatially correlated with the expression profiles of myelin basic protein (Supplementary Fig. 5c–f), a major constituent of myelin sheath[31], and temporally coincide with the restricted myelination window during development[32]. Thus, our observation supports previous findings that myelination requires high levels of lipid synthesis during the developmental period[33]. Besides brain, we also obtained other tissues from the young mouse, including pancreas,

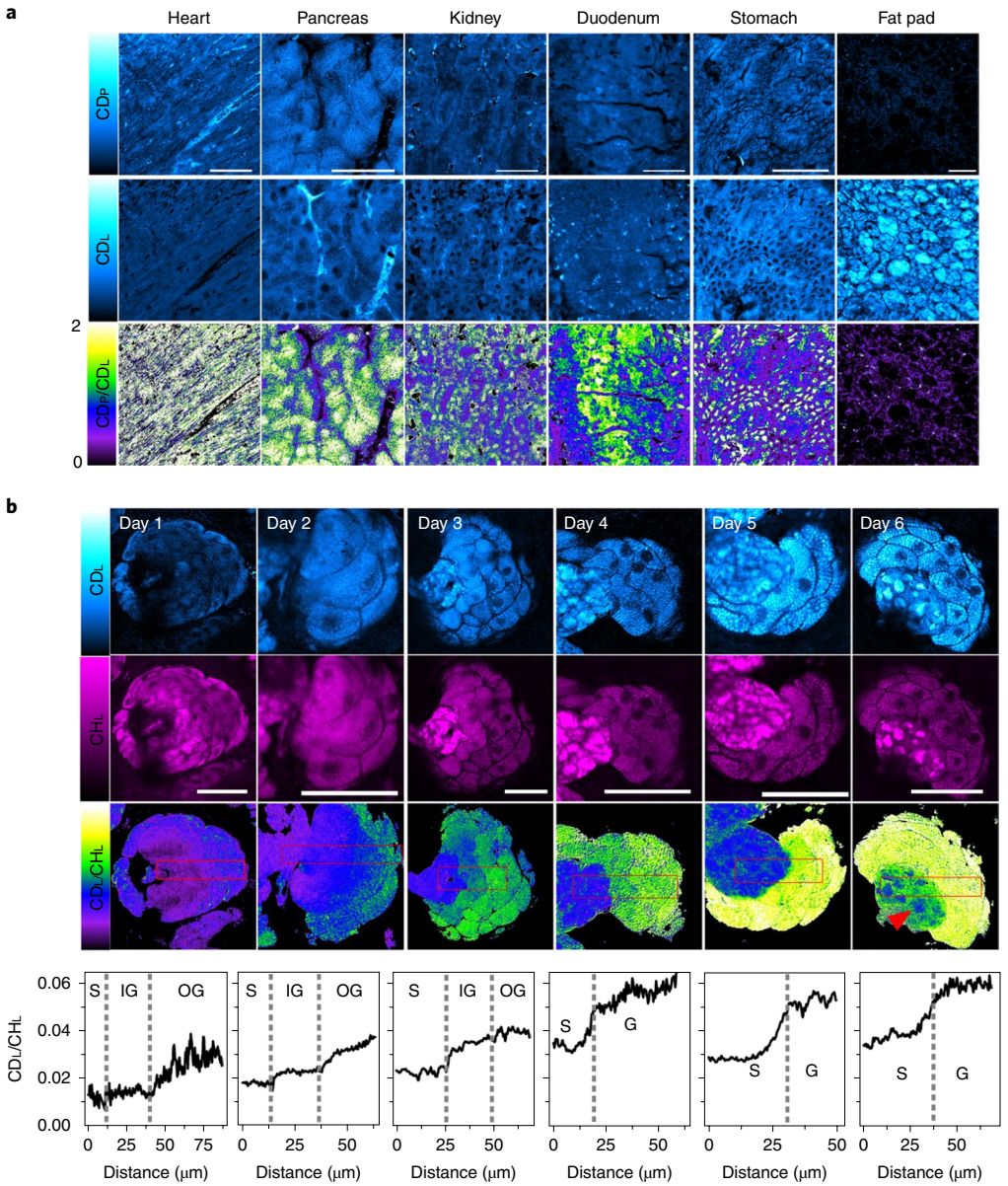

Fig. 4 | STRIDE imaging in mouse tissue. a, Unmixed CD_L and CD_P images of various tissue slices from mouse (P30) after drinking 10% [D_7]-glucose for 10 d. Ratiometric images were calculated as CD_P/CD_L to represent functional divergence of glucose utilization. **b**, Time-dependent tracking of CD_L and CH_L images of the sebaceous gland from a mouse drinking 5% [D_7]-glucose water for 1–6 d. Ratiometric images were calculated as CD_L/CH_L to represent lipid turnover dynamics. Arrows indicate remnants of sebocytes. Line profiles for the areas outlined in red (bottom). Dashed lines indicate boundaries identified by morphology. S, sebum; IG, inner gland; OG, outer gland; G, gland. Scale bars, 50 μm.

heart, muscle, lung, kidney, stomach and fat pad, and used these to compile a tissue atlas of metabolic activity (Supplementary Fig. 5g). Of note, a clearly higher protein synthesis activity was observed in brown adipose tissue (marked by its smaller lipid droplet size) compared with white adipose tissue, indicating more diverse utilization of glucose, possibly to fulfill the various secretion roles of brown adipose cells[34] (Supplementary Fig. 5g).

A hallmark of tumour metabolism is the marked upregulation of glucose metabolism[3,15]. We therefore applied STRIDE imaging to assess macromolecule synthesis in xenograft tumour mouse models. We administered [D_7]-glucose drinking water to mice for 30–40 d after injection of U87MG brain glioblastoma xenograft[35]. After collecting brain tissue slices containing the solid tumour (Supplementary Fig. 5h), we identified the tumour regions based on the basis of position of implantation as well as hypercellularity according to label-free SRS histology[29,35] (Supplementary Fig. 5i). As expected, compared with the normal brain tissue across the boundary, both lipid and protein synthesis were more active in tumours, according to the CD_L/CH_L and CD_P/CH_P ratio images (Supplementary Fig. 5j). Furthermore, the CD_P/CD_L image showed that utilization of glucose was also different in tumours, with increased protein synthesis from glucose.

STRIDE imaging lipid absorption in neonatal intestine. In the small intestine of the young mouse (E11–P21) but not the adult mouse, we observed a surprisingly large signal in globule structures with diameter up to 3 μm (Fig. 6a). As this is likely to be a steady-state result after long-term labelling, the true spatiotemporal dynamics remain hidden. We therefore shortened the administration period of [D_7]-glucose drinking water to 5 h for the lactating

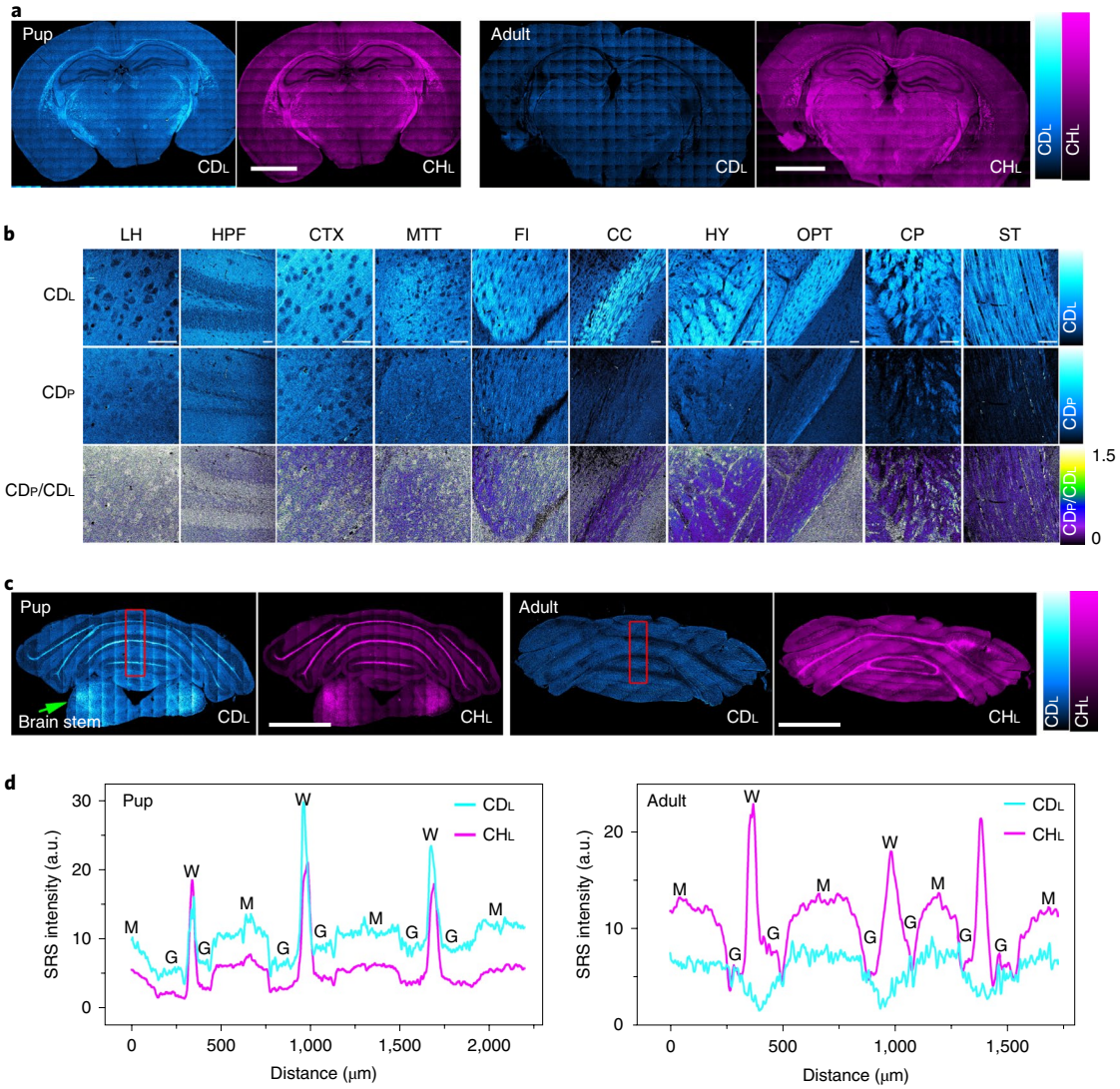

Fig. 5 | STRIDE imaging of protein and lipid biosynthesis in mouse brain. a, Imaging lipid (CD_L) and protein (CD_P synthesis in cerebrum of pups (P21) and adult mice (P100). Pup mice were labelled with 2% [D_7]-glucose during the developmental period (E11 to P21) via the mother's drinking water. Adult mice were labelled with 2% [D_7]-glucose for 30 d. Unlabelled lipid (CH_L) and protein (CH_P) are also shown. **b**, Magnified images from different areas in **a**. Ratiometric images were calculated as CD_P/CD_L. CTX, cortex. **c**, Imaging lipid (CD_L) synthesis in cerebellum of same pup and adult mice as in **a**. **d**, Line profiles of lipid synthesis (CD_L) and unlabelled lipid (CH_L) shown for the boxed area in **c**. M, molecular layer; G, granule cell layer; W, white matter. Scale bars, 2 mm (**a**,**c**) and 50 μm (**b**).

mother, and restricted subsequent of the pup to 15 min. Early radioisotope measurement on suckling rodents suggested that there was a time lag of about 30 min between nutrient supplementation and intestinal absorption, but this could not be confirmed due to poor detectability at early time points[36]. However, even within 15 min after feeding, we observed an intense C–D signal in the villi of the small intestine of the pup (Fig. 6b, quantification in Supplementary Table 3), indicating efficient nutrient absorption and processing by the neonatal intestinal epithelium. The globular structures indicated by the signal are dominated by signal in the CD_L channel and can be stained with Nile red, a stain for neutral lipid (Fig. 6b), suggesting they are intracellular lipid droplets or assembled chylomicrons. Indeed, fat accounts for nearly half the dry mass of milk, and milk fat is the major nutrient for the suckling pup[37,38].

We then captured spatially unidirectional fat synthesis and repackaging in neonatal mouse intestine. Nutrient absorption across intestinal epithelium is primarily carried out by enterocytes[39]. These highly polarized cells take up nutrients at their brush boarder surface and transport them across the basal membrane where the nutrients enter the circulation in the villi. Using the optical-sectioning ability of SRS, we obtained depth-resolved images from the brush-border surface deep into the villi (Fig. 6c,d), clearly revealing depth dependence of droplet size (Fig. 6e). From the apical surface, where absorption of milk fats takes place, through the cytoplasm of the enterocyte to the capillary and lacteal network, below which chylomicrons are secreted, the diameter of the largest droplet increases from 1.6 μm to 2.9 μm, indicating unidirectional fat synthesis and repackaging from the apical surface to the basal membrane of the enterocytes. In sum, STRIDE microscopy provides high spatiotemporal resolution for direct visualization of maternal nutrient transfer, and reveals the highly efficient and unidirectional process of fat absorption and processing by the neonatal intestinal epithelium.

STRIDE imaging of glucose isotopologues for temporally resolved metabolic dynamics. Pulse–chase analysis is an established approach to dissecting the temporal progression of biological

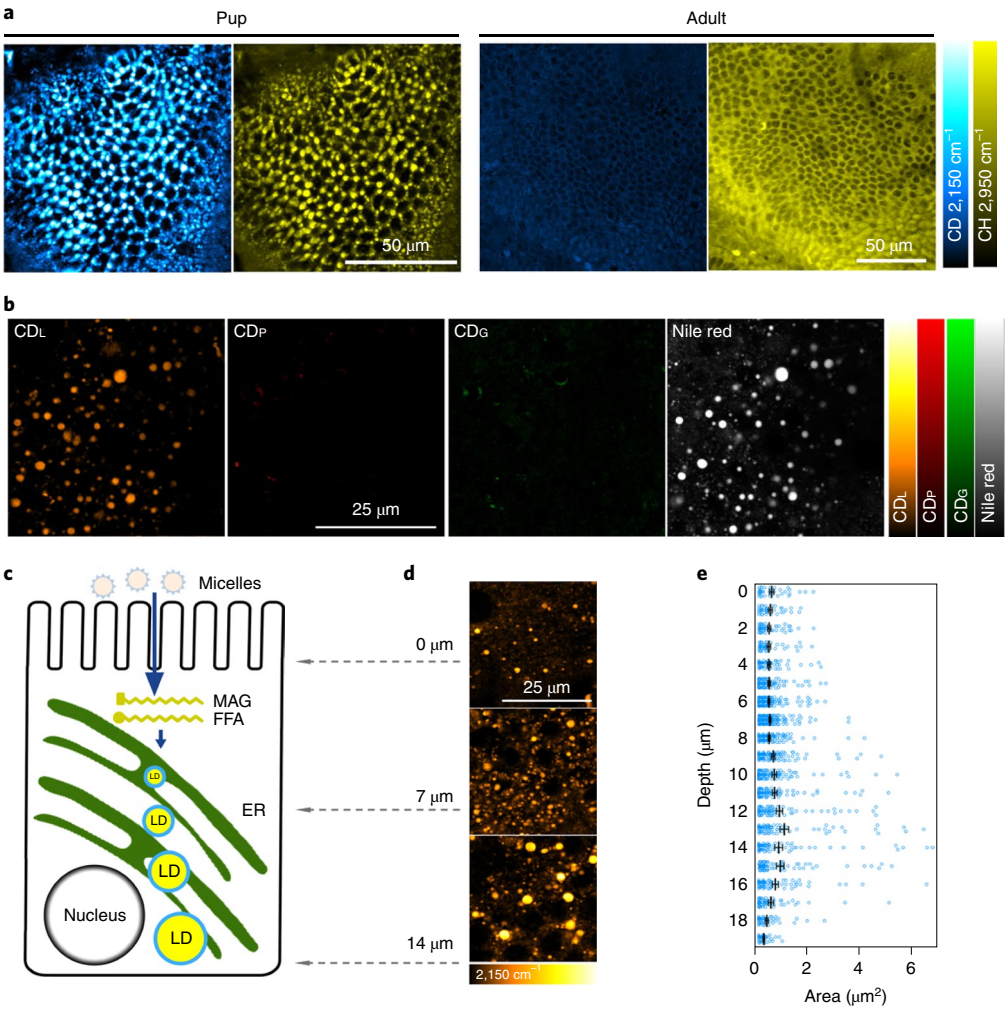

Fig. 6 | STRIDE imaging reveals fast and unidirectional lipid absorption in newborn mouse intestine. a, Images of intestinal epithelium (duodenum) from the same pup and adult as in Fig. 4a. C–D and C–H images represent glucose-derived signal and unlabelled biomass signal, respectively. **b**, Images of intestinal epithelium (duodenum) from a pup (P10) after 15 min feeding with milk from a lactating mouse administered 10% [D_7]-glucose for 5 h. Images show separation of glucose-derived C–D signal into lipid (CD_L), protein (CD_P) and glycogen (CD_G) channels, and correlative Nile red confocal fluorescence of the stained tissue. **c**, Illustration of fat absorption across the enterocyte of intestinal epithelium. MAG, monoacylglyceride; FFA, free fatty acid; LD, lipid droplet; ER, endoplasmic reticulum. **d**, Images of glucose-derived lipid synthesis acquired at different depth across the intestinal enterocyte. **e**, Quantitative analysis of depth profile of lipid-droplet size distribution. Data are presented as scatter plots for individual lipid droplets and shown as mean ± s.e.m.

processes. The versatility of probes has enabled pulse–chase assessments in complex settings by labelling different time intervals with probes with distinct colours[40–42]. We sought to investigate whether STRIDE could be developed into a pulse–chase labelling system with orthogonal glucose probes, on the basis of multiple partially labelled glucose isotopologues beyond the fully deuterated [D_7]-glucose described above. We observed the diverging fates and environment of the seven deuterium atoms in [D_7]-glucose (Fig. 2a); this divergence underlies the rationale of mass spectrometric analysis, which uses partially deuterium-labelled glucose isotopologues to highlight specific metabolic pathways[43,44]. Inspired by this strategy and realizing the sensitivity of STRIDE to deuterium labelling pattern and chemical environment, we speculated that Raman spectra of macromolecule metabolites may also encode the origin of glucose isotopologues.

We began with glycogen, which retains the most deuterium from glucose. We obtained the Raman spectrum of liver glycogen derived from [6,6-D_2]-glucose (hereafter [D_2]-glucose), which indeed showed pronounced difference compared with that derived from [D_7]-glucose (Fig. 7a and Supplementary Fig. 6a). We then obtained Raman spectra of lipids and proteins extracted from HeLa cells cultured in [D_7]-glucose, [D_2]-glucose or [1-D_1]-glucose (normalized at 1,450 cm^{-1} for lipid and 1,670 cm^{-1} for protein). The spectra derived from each glucose isotopologue showed apparent differences not only in overall intensity but also in the relative intensities at multiple frequencies (Fig. 7b,c). Further insights into pathway-specific contributions can be gained by analysing the intensity and assigning peak frequencies in these spectra (see Supplementary Information). Therefore, on the basis of the clearly distinguishable spectra of macromolecules derived from [D_7]-glucose and [D_2]-glucose, we selected these two isotopologues as orthogonal probes to label temporally separated populations within the same sample.

As a proof-of-concept demonstration of pulse–chase labelling and imaging, we sequentially administered [D_7]-glucose and [D_2]-glucose (each for 24 h) in the drinking water of a mouse and collected the skin tissue, in which glucose is used almost exclusively for lipid synthesis in sebaceous glands. After linear unmixing based on the lipid spectra derived from the two isotopologues (Supplementary Fig. 6b), we successfully visualized de novo lipid synthesis in these two successive time windows. Spatial segregation

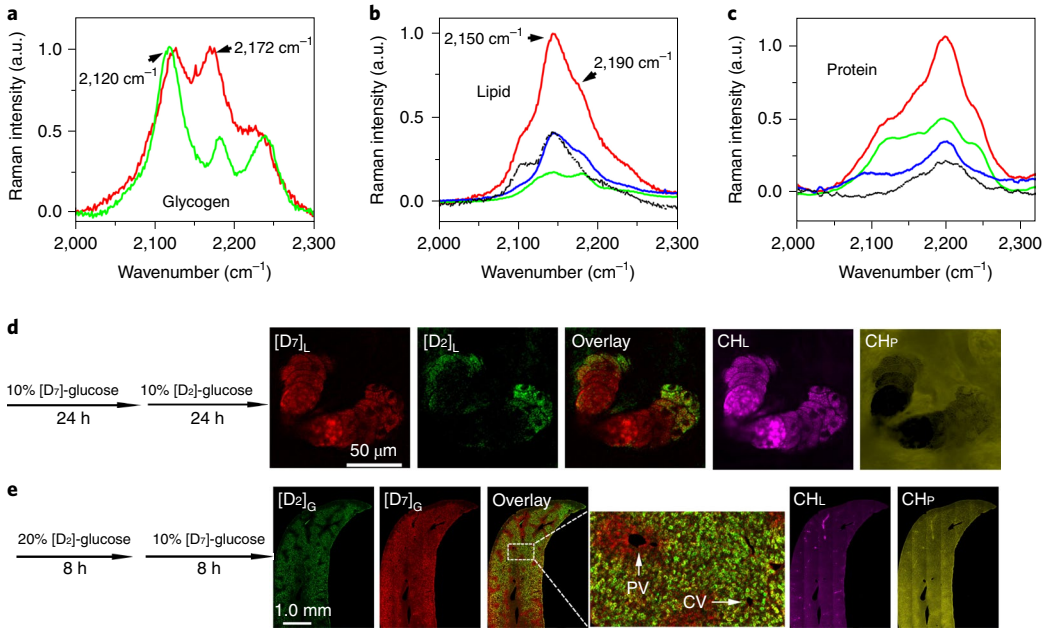

Fig. 7 | Pulse–chase STRIDE imaging of metabolic dynamics through sequentially labelled [D_7]- and [D_2]- glucose. a, C–D Raman spectra of liver glycogen derived from mice fed with [D_7]-glucose or [6,6-D_2]-glucose. Overnight-fasted mice were stimulated and labelled with 10% [D_7]-glucose or [6,6-D_2]-glucose for 8 h, and liver tissues were used for Raman spectra acquisition. Red, [D_7]-glucose-fed mouse; green, [6,6-D_2]-glucose-fed mouse. **b**, Raman spectra of lipid extracts from HeLa cells cultured with 0.45% [D_7]-glucose, [6,6-D_2]-glucose or [1-D_1]-glucose for 6 d, and normalized at 1,450 cm^{-1} (lipid C–H bending). Red, from [D_7]-glucose-cultured cell; green, from [6,6-D_2]-glucose-cultured cell; blue, from [1-D_1]-glucose. The black dashed curve is calculated by subtracting the [6,6-D_2]-glucose-derived signal and the [1-D_1]-glucose-derived signal from the [D_7]-derived signal. **c**, Raman spectra of protein extracts from HeLa cells cultured with 0.45% [D_7]-glucose, [6,6-D_2]-glucose or [1-D_1]-glucose for 6 d. Normalized at 1,670 cm^{-1} (protein amide I band). Red, [D_7]-glucose; green, [6,6-D_2]-glucose; blue, [1-D_1]-glucose. The black dashed curve is calculated by subtracting the [6,6-D_2]-glucose- and [1-D_1]-glucose-derived signals from the [D_7]-derived signal. **d**, Unmixed images of lipid signal derived from 10% [D_7]-glucose ($[D7]_L$) and [6,6-D_2]-glucose ($[D2]_L$) labelling in successive 24 h time windows in mouse. Images were taken from the sebaceous gland of ear skin. Overlay of $[D7]_L$ and $[D2]_L$ channels show different spatial distribution. Unlabelled lipid (CH_L) and protein (CH_P) are also shown. **e**, Unmixed images of glycogen signal derived from 20% [D_2]-glucose ($[D2]_G$) and 10% [D_7]-glucose ($[D7]_G$) labelling in successive 8 h time windows in overnight-fasted mice. Images were taken from a liver tissue slice. Overlay of $[D2]_G$ and $[D7]_G$ channels show different spatial distribution. Portal vein (PV) and central vein (CV) are discerned by the existence of a triad structure.

of lipids synthesized earlier and later in time was evident in sebaceous glands (Fig. 7d): compared with the later pool, the earlier pool migrated closer to the secreting duct in the centre, consistent with the gradient observed in Fig. 4b.

Similarly, pulse–chase labelling can be used to assess glycogen accumulation in liver. The mouse liver is divided into basic functional units termed lobules, inside which a general nutrient gradient can be observed from portal vein to central vein. Liver metabolic functions are found to be zonated across the nutrient gradient; this zoning is increasingly important in understanding liver architecture[5]. We sequentially administered [D_2]-glucose and [D_7]-glucose (for 8 h each) in the drinking water of a mouse fasted overnight. The acute labelling scheme highlights glycogen synthesis in liver without interference from basal-level synthesis of other metabolites (Supplementary Fig. 6c). Applying spectral unmixing, we successfully separated signals of glycogen synthesis derived from the two glucose isotopologues (Supplementary Fig. 6d–f) and observed the spatial patterns in the signals (Fig. 7e). In general, the label that was administered second (red) appears throughout the liver lobule, whereas the first label (green) accumulates more in the pericentral zone and becomes depleted around the portal vein. Such a pattern supports the reported faster glycogen turnover in the periportal zone[45]. Compared with traditional methods of glycogen staining[45] or isolating zonated cells[46], the pulse–chase approach reveals explicit spatial distribution of glycogen synthesized during different time windows within the same liver tissue, avoiding the complication of pre-existing pools or cross-sample variation. The spatial information offered in situ also better reflects zonation in large-scale tissue organization. Metabolic heterogeneity among single cells is also evident from the scattered distribution of cells actively accumulating glycogen (Fig. 7e). With this unmatched spatial resolution for revealing single-cell heterogeneity, STRIDE will be useful for metabolic phenotyping in the era of single-cell omics.

Discussion

We have detected distinct Raman spectral fingerprints for C–D bonds in macromolecules derived from [D]-glucose, and harnessed them for macromolecule-type-specific metabolic mapping with high spatial resolution. We further exploited C–D Raman spectral fingerprints for spectrally separating deuterium-labelled macromolecules derived from different glucose isotopologues, which enabled two-colour pulse–chase probing in different temporal windows and revealed metabolic gradients in sebaceous gland and liver. In this current demonstration, we mostly focused on macromolecule-type-specific imaging. Although the chemical information may be limited compared with other metabolic tracing and imaging techniques such as NMR or mass spectrometry, STRIDE offers high spatial resolution in a nondestructive fashion to meet the growing demand of mapping tissue metabolic heterogeneity, thereby complementing the current toolkit for assessing metabolic dynamics in animals.

The C–D bond has been increasingly adopted in Raman microscopy as a vibrational tag for imaging metabolic incorporation of

precursor molecules[21,23]. The C–D bonds in the final biomaterial are usually detected at the same frequency as in the precursor molecule. In other words, one precursor molecule corresponds to one detection channel, thus limiting monitoring to one type of metabolism at a time. This one-to-one correspondence could be extended to multiple probes[26,42,47], but is in most cases still limited to a single type of metabolism as a targeted imaging approach. Conceptually, STRIDE of glucose metabolism is different from previously reported deuterium-labelled metabolic precursor labelling. It is based on the central metabolic role of glucose, and extends the chemical information derived from a single probe to multiplexed imaging of glucose metabolites. This is realized by acknowledging the diverse chemical environment in macromolecules. In other words, in STRIDE, the C–D bond is not only a concentration probe for overall metabolic activity, but also a local sensor for macromolecule identity. This conceptual feature also distinguishes STRIDE from earlier attempts at single-channel glucose metabolic imaging (mostly reporting lipid synthesis) in bacteria or cultured cells[24,25,48–50].

STRIDE imaging has broad potential applications, ranging from general assessment of glucose anabolic utilization to visualization of metabolic activity of specialized organs like adipose, pancreas or liver. Depending on the specific applications, the concentration and duration of [D]-glucose administration can be further optimized. In this general demonstration, we administered glucose in drinking water in the concentration range of 2–10% to reveal tissues with low metabolic activity. Glucose, as a nutrient source, is likely to alter metabolism systematically. We therefore measured food and water intake, body weight gain and glucose tolerance in mice with or without drinking 10% glucose for 10 d (Supplementary Table 2). Though long-term administration of glucose reduces food intake, no observable perturbation to glucose tolerance was observed. Moreover, the concentration and/or labelling duration can be effectively reduced if a particular process is of interest. The detection limit is set by two factors: deuterium-label incorporation and detection sensitivity of SRS. Only a limited number of deuterium molecules is incorporated into biomass—most are lost during glycolysis and energy production. At least 10 mM C–D bonds, corresponding to 0.1–1% deuterium enrichment in macromolecules, is required for SRS imaging at high spatial resolution. Quantitatively, we have summarized the detected signal-to-noise ratio (for 100 µs pixel-dwell time) in some specialized tissues and the corresponding labelling condition (Supplementary Table 3). For example, adipose tissue obtained from mice drinking 10% glucose for 10 d exhibits a signal-to-noise ratio of 570 ± 90 and liver glycogen obtained from acutely treated mice (10% glucose, 8 h) exhibit a signal-to-noise ratio of 44 ± 24. On the basis of these quantifications, there is further room for parameter optimization.

Although most images were acquired from tissue slices in transmission mode, the labelling and optical detection are non-invasive, allowing the imaging of a live mouse (Fig. 1e and Supplementary Video 1). The current imaging depth is comparable to that of typical two-photon fluorescence microscopy (hundreds of micrometres); thus, for imaging internal organs, post mortem tissue sectioning is still required. We envision the applicability of this technique in vivo with instrumentation upgrade to epi-detected SRS and to the recently developed coherent Raman scattering endoscope[51,52].

Methods

Materials. Metabolic labelling was achieved with [D_7]-glucose, [6,6-D_2]-glucose (Cambridge Isotope) and [1-D_1]-glucose (Sigma-Aldrich). Spectra were assigned using standards including fatty acids, [12-D_1]-palmitic acid (Cambridge Isotope, dissolved in DMSO), [U-D_{31}]-palmitic acid (Sigma-Aldrich, dissolved in DMSO); amino acids, [2,3,3,3-D_4]-alanine, [D_8]-valine (Cambridge Isotope, dissolved in PBS) and [U-D_8]-glycerol (Cambridge Isotope). Glucose uptake was measured using 3-*O*-propargyl-D-glucose as described[12]. TVB-3166 (Sigma-Aldrich) was used to inhibit fatty acid synthesis. Perchloric acid (Fisher Scientific) was used to remove glycogen in tissue.

Cell culture, labelling and imaging. Cell lines used in this study are PC3 (ATCC), HeLa (ATCC), MCF7 (ATCC), RWPE-1 (ATCC) and U87MG (ATCC). Cell cultures were maintained according to the instructions from ATCC in the designated medium. For labelling cell culture, medium was replaced with glucose-free DMEM (ThermoFisher, catalogue no.11966) supplemented with [D_7]-glucose (0.45%, w/v). For DNA labelling, serum was reduced to 5% in culture. For acquisition of spectra of isolated macromolecules, serum was reduced to 2% in culture to increase labelling efficiency. For live imaging, cells were plated onto a glass-bottomed dish (MATTEK). For imaging fixed-cell imaging, cells were plated onto coverslips (No. 1, FisherBrand). Cells were first cultured in regular medium and then switched to [D_7]-glucose-substituted medium for the designated duration. Following imaging, the medium was replaced with PBS or cells were fixed with 4% PFA for 30 min, and the coverslip was sandwiched onto a glass slide (1 mm thick, VWR) with an imaging spacer (0.12 mm thick, SecureSeal).

Macromolecule isolation from cultured cells. Hela cells were first cultured in 25 cm^2 culture flask in complete medium to 50% confluence. The medium was then replaced with DMEM substituted with 0.45% [1-D_1]-glucose, [6,6-D_2]-glucose or [D_7]-glucose with 2% fetal bovine serum. The medium was replaced with fresh medium every 2 d. After 6 d, cells were dissociated and collected, and DNA, RNA and proteins were extracted using TRIzol Reagent (ThermoFisher) according to the manufacturer's instructions. For lipid extraction, cells were collected and suspended in 1 ml PBS and mixed with 1.3 ml chloroform and 2.7 ml methanol. The solution was centrifuged at 4,000 r.p.m. for 5 min. The supernatant was transferred to a new clean tube, and mixed with 1 ml of 50 mM citric acid (Sigma-Aldrich), 2 ml distilled water and 1 ml chloroform. After briefly shaking and mixing, the tube was centrifuged at 4,000 r.p.m. for 10 min. The material separated into three phases: a water–methanol upper phase, a middle phase of precipitated protein and a lower chloroform phase. Lipids were dissolved in the lower chloroform phase. The chloroform phase was separated, dropped on a cover glass and air-dried.

Mouse labelling. All animal experiments were conducted in adherence with the experimental protocol approved by the Institutional Animal Care and Use Committee (AC-AAAQ0496). For normal conditions, wild-type (strain C57BL/6J, Jackson Laboratory) mice were given drinking water containing [D_7] or [6,6-D_2]-glucose at the designed concentration. Mice had free access to regular chow during this time. For overnight fasting, mice were fasted for 18 h with access to regular drinking water only. For labelling embryonic or neonatal mice, [D_7]-glucose was administered to the pregnant or lactating wild-type female mouse in their drinking water. For labelling and imaging in skin sebaceous gland, nude mice (strain J:NU, Jackson Laboratory) were used to avoid strong absorption of pigment. The ear skin was either clipped or directly imaged in the live mouse.

Mouse tumour xenograft. Orthotopic brain glioblastoma xenograft was established by intracranial implantation of U87MG human glioma cells. In brief, nude mice (strain J:NU, Jackson Laboratory) were anaesthetized and positioned in a stereotaxic instrument (David Kopf Instruments). A small section (2 mm in diameter) of the skull was ground with a dental drill (Braintree Scientific) until it became soft and translucent. Subsequently, 1.5×10^5 U87MG tumour cells (in 3 µl) were injected into the frontal region of the cerebral cortex over the course of 5 min using a 1.5 mm glass capillary. After the implantation, mouse head skin was closed with silk sutures (Harvard Apparatus).

Tissue slicing. After treatment and labelling, the mice were anaesthetized, killed by cervical dislocation and organs were collected. The tissues were fixed with PFA for more than 48 h after collection. Tissues were then embedded in 4% agarose gel (Sigma-Aldrich), and sliced into 100 µm thin slices using a vibratome (Leica). Brain was sliced coronally. Random orientation was used for other tissues. The tissue slices were collected and sealed between a glass slide and coverslip.

Tissue processing. To remove lipid, tissue slices were soaked in pure methanol for 48 h and then washed with PBS. To remove glycogen, liver slices were incubated in ice-cold 10% perchloric acid for 1 h and then washed with PBS. To extract lipid from adipose tissue, 1 g of adipose tissues were collected, ground and suspended in 1 ml PBS, and then mixed with 2.6 ml chloroform and 5.4 ml methanol. The suspension was centrifuged at 4,000 r.p.m. for 5 min. The supernatant was transferred to a new clean tube and mixed with 2 ml of 50 mM citric acid (Sigma-Aldrich), 4 ml water and 2 ml chloroform. After brief shaking and mixing, the tube was centrifuged at 4,000 r.p.m. for 10 min to separate the phases. The lower chloroform phase containing lipids was collected and solvent was evaporated to obtain tissue lipid extract.

NMR. NMR spectra were recorded on a Bruker 500 (500 MHz) or Bruker 400 (400 MHz) Fourier transform NMR spectrometer. Lipids extracted from the mouse adipose tissues were dried and weighted, and dissolved in 600 µl chloroform

and 2 µl deuterated chloroform (Cambridge Isotope) to obtain deuterium-NMR spectra. To obtain hydrogen-NMR spectra the lipid extract was re-dissolved in 700 µl deuterated chloroform 10 µl chloroform. The two spectra were calibrated and normalized according to the chloroform (δ 7.26 ppm) for quantitative estimation of the deuterium substituted ratio.

Spontaneous Raman spectroscopy. Raman spectra were obtained from fixed cells or tissue as previously described[53]. In brief, samples were placed on an upright confocal Raman microspectrometer (Xplora, Horiba Jobin Yvon) equipped with a 532 nm diode laser source and 1,800 lines per mm grating at room temperature. The excitation power was ~42 mW after passing through a ×50 air objective (MPlan N, 0.75 numerical aperture, Olympus), and 60 s acquisition time was used to collect Raman spectra of all samples at a single point under identical conditions. For cultured cells, the Raman background of water and cover glass is removed by subtracting the signal in cell-free areas from the signal collected in cells. For tissue with detectable autofluorescence background such as liver, the acquisition spot on the tissue was first photobleached by the laser for several minutes before spectra acquisition.

SRS microscopy. Similar to a previously described setup[54], we used an inverted laser-scanning microscope (FV1200, Olympus) optimized for near-infrared throughput and a ×25 water objective (XLPlanN, 1.05 numerical aperture, MP, Olympus) with high near-infrared transmission for SRS imaging. A picoEMERALD system (Applied Physics & Electronics) supplied a synchronized-pulse pump beam (with tunable 720–990 nm wavelength, 5–6 ps pulse width and 80 MHz repetition rate) and Stokes beam (with fixed wavelength at 1064 nm, 6 ps pulse width and 80 MHz repetition rate). The Stokes beam was modulated at 8 MHz by an electronic optic modulator. Transmission of the forward-going pump and Stokes beams after passing through the samples was collected by a high numerical aperture (1.4) oil condenser. A high optical density bandpass filter (890/220, Chroma) was used to block the Stokes beam completely and to transmit only the pump beam onto a large area Si photodiode for the detection of the stimulated Raman loss signal. The output current from the photodiode was terminated, filtered and demodulated with a lock-in amplifier (Zurich, HF2LI) at 8 MHz to ensure shot-noise-limited detection sensitivity. The demodulated signal was fed into the analogue channel of FV1200 software FluoView 4.1a (Olympus) to form an image during laser scanning at a rate of 100 µs per pixel. For multichannel SRS imaging, the pump wavelength (λ_{pump}) was tuned so that the energy difference between pump and Stokes beams matched with the vibrational frequency as described by the equation

$$\lambda_{pump} = \frac{1}{\frac{1}{1,064} + 10^{-7} \times \nu}$$

where ν is the vibrational frequency in cm^{-1}. C–D channels were acquired at the frequencies shown in each figure. C–H channels were acquired at 2,845 cm^{-1} and 2,940 cm^{-1} and unmixed as described[55].

In vivo imaging of mouse ear skin. A nude mouse was given 5% [D_7]-glucose in drinking water and regular chow for 8 d before imaging. The mouse was then kept anaesthetized with isoflurane while one ear was gently sandwiched between a coverslip and a glass slide, which were then placed onto the imaging stage with a heated pad under the mouse to maintain its body temperature during the imaging session. A faster scanning rate (1.6 s per frame) was used for live imaging.

Nile red confocal fluorescence. Small intestine tissue slices were stained with 1 µM Nile red (Invitrogen) for 1 h. The tissue was then washed and imaged using confocal fluorescence in the same microscope used for SRS imaging. The excitation wavelength and filter were 488 nm and 505–605 nm, respectively.

Software. Images were processed and pseudocoloured in ImageJ. For SRS images of C–D channels, corresponding off-resonance images were taken at 1,900 cm^{-1} and subtracted from the on-resonance images. Stimulated Raman histology was generated according to the reported procedure[29]. In brief, the protein channel ($I_{2,940} - I_{2,845}$) was assigned a haematoxylin-like blue colour, while the lipid channel ($I_{2,845}$) was assigned an eosin-like pink colour, and the two channels were merged; where I represents SRS intensity. Quantification of droplet size in intestinal tissue was done by applying automatic local thresholding and analysing particles to the depth-resolved image stack. Data analysis and visualization were done in GraphPad and Origin software.

Reporting Summary. Further information on research design is available in the Nature Research Reporting Summary linked to this article.

Data availability

The authors declare that all data supporting the results of this study are available within the paper and its Supplementary Information. All raw and processed images generated in this work are available from the corresponding author on reasonable request.

Received: 15 May 2018; Accepted: 17 March 2019;
Published online: 29 April 2019

References

1. Saltiel, A. R. & Kahn, C. R. Insulin signalling and the regulation of glucose and lipid metabolism. *Nature* **414**, 799–806 (2001).
2. Hensley, C. T. et al. Metabolic heterogeneity in human lung tumors. *Cell* **164**, 681–694 (2016).
3. Vander Heiden, M. G. & DeBerardinis, R. J. Understanding the intersections between metabolism and cancer biology. *Cell* **168**, 657–669 (2017).
4. Pipeleers, D. G. Heterogeneity in pancreatic β-cell population. *Diabetes* **41**, 777–781 (1992).
5. Halpern, K. B. et al. Single-cell spatial reconstruction reveals global division of labour in the mammalian liver. *Nature* **542**, 1–5 (2017).
6. Gambhir, S. S. Molecular imaging of cancer with positron emission tomography. *Nat. Rev. Cancer* **2**, 683–693 (2002).
7. Walker-Samuel, S. et al. In vivo imaging of glucose uptake and metabolism in tumors. *Nat. Med.* **19**, 1067–1072 (2013).
8. Rodrigues, T. B. et al. Magnetic resonance imaging of tumor glycolysis using hyperpolarized ^{13}C-labeled glucose. *Nat. Med.* **20**, 93–97 (2013).
9. Sugiura, Y. et al. Visualization of in vivo metabolic flows reveals accelerated utilization of glucose and lactate in penumbra of ischemic heart. *Sci. Rep.* **6**, 32361 (2016).
10. Guillermier, C., Poczatek, J. C., Taylor, W. R. & Steinhauser, M. L. Quantitative imaging of deuterated metabolic tracers in biological tissues with nanoscale secondary ion mass spectrometry. *Int. J. Mass Spectrom.* **422**, 42–50 (2017).
11. Zou, C., Wang, Y. & Shen, Z. 2-NBDG as a fluorescent indicator for direct glucose uptake measurement. *J. Biochem. Biophys. Methods* **64**, 207–215 (2005).
12. Hu, F. et al. Vibrational imaging of glucose uptake activity in live cells and tissues by stimulated Raman scattering. *Angew. Chem. Int. Ed.* **54**, 9821–9825 (2015).
13. Nelson, D. & Cox, M. *Lehninger Principles of Biochemistry* 4th edn (W. H. Freeman, 2005).
14. Chen, Y. J. et al. Differential incorporation of glucose into biomass during Warburg metabolism. *Biochemistry* **53**, 4755–4757 (2014).
15. Lunt, S. Y. & Vander Heiden, M. G. Aerobic glycolysis: meeting the metabolic requirements of cell proliferation. *Annu. Rev. Cell Dev. Biol.* **27**, 441–464 (2011).
16. Otero, Y. F., Stafford, J. M. & McGuinness, O. P. Pathway-selective insulin resistance and metabolic disease: the importance of nutrient flux. *J. Biol. Chem.* **289**, 20462–20469 (2014).
17. Uyeda, K. & Repa, J. J. Carbohydrate response element binding protein, ChREBP, a transcription factor coupling hepatic glucose utilization and lipid synthesis. *Cell Metab.* **4**, 107–110 (2006).
18. Freudiger, C. W. et al. Label-free biomedical imaging with high sensitivity by stimulated Raman scattering microscopy. *Science* **322**, 1857–1861 (2008).
19. Min, W., Freudiger, C. W., Lu, S. & Xie, X. S. Coherent nonlinear optical imaging: beyond fluorescence microscopy. *Annu. Rev. Phys. Chem.* **62**, 507–530 (2011).
20. Chung, C.-Y. & Potma, E. O. Biomolecular imaging with coherent nonlinear vibrational microscopy. *Annu. Rev. Phys. Chem.* **64**, 77–99 (2013).
21. Cheng, J.-X. & Xie, X. S. Vibrational spectroscopic imaging of living systems: an emerging platform for biology and medicine. *Science* **350**, aaa8870 (2015).
22. Zhao, Z., Shen, Y., Hu, F. & Min, W. Applications of vibrational tags in biological imaging by Raman microscopy. *Analyst* **142**, 4018–4029 (2017).
23. Wei, L. et al. Live-cell bioorthogonal chemical imaging: stimulated Raman scattering microscopy of vibrational probes. *Acc. Chem. Res.* **49**, 1494–1502 (2016).
24. Li, M., Huang, W. E., Gibson, C. M., Fowler, P. W. & Jousset, A. Stable isotope probing and Raman spectroscopy for monitoring carbon flow in a food chain and revealing metabolic pathway. *Anal. Chem.* **85**, 1642–1649 (2013).
25. Li, J. & Cheng, J.-X. Direct visualization of de novo lipogenesis in single living cells. *Sci. Rep.* **4**, 6807 (2015).
26. Long, R. et al. Two-color vibrational imaging of glucose metabolism by stimulated Raman scattering. *Chem Commun.* **54**, 152–155 (2017).
27. Sun, R. C. et al. Noninvasive liquid diet delivery of stable isotopes into mouse models for deep metabolic network tracing. *Nat. Commun.* **8**, 1646 (2017).
28. Longhi, G., Zerbi, G., Paterlini, G., Ricard, L. & Abbate, S. Conformational dependence of CH(CD)-strechings in D-glucose and some deuterated derivatives as revealed by infrared and Raman spectroscopy. *Carbohydr. Res.* **161**, 1–22 (1987).
29. Orringer, D. A. et al. Rapid intraoperative histology of unprocessed surgical specimens via fibre-laser-based stimulated Raman scattering microscopy. *Nat. Biomed. Eng.***1**, 0027 (2017).
30. Jung, Y., Tam, J., Jalian, H. R., Anderson, R. R. & Evans, C. L. Longitudinal, 3D in vivo imaging of sebaceous glands by coherent anti-stokes Raman scattering microscopy: normal function and response to cryotherapy. *J. Invest. Dermatol.* **135**, 39–44 (2015).

31. Yoshikawa, F. et al. Opalin, a transmembrane sialylglycoprotein located in the central nervous system myelin paranodal loop membrane. *J. Biol. Chem.* **283**, 20830–20840 (2008).
32. Bercury, K. K. & Macklin, W. B. Dynamics and mechanisms of CNS myelination. *Dev. Cell* **32**, 447–458 (2015).
33. Jurevics, H. & Morell, P. Cholesterol for synthesis of myelin is made locally, not imported into brain. *J. Neurochem.* **64**, 895–901 (1995).
34. Cannon, B. & Nedergaard, J. Brown adipose tissue: function and physiological significance. *Physiol. Rev.* **84**, 277–359 (2004).
35. Brehar, F. M. et al. The development of xenograft glioblastoma implants in nude mice brain. *J. Med. Life* **1**, 275–286 (2008).
36. Flores, C. A., Hing, S. A., Wells, M. A. & Koldovsky, O. Rates of triolein absorption in suckling and adult rats. *Am. J. Physiol. Liver Physiol.* **257**, G823–G829 (1989).
37. Lindquist, S. & Hernell, O. Lipid digestion and absorption in early life: an update. *Curr. Opin. Clin. Nutr. Metab. Care* **13**, 314–320 (2010).
38. Pácha, J. Development of intestinal transport function in mammals. *Physiol. Rev.* **80**, 1633–1667 (2000).
39. Alberts, B. et al. *Molecular Biology of the Cell* 4th edn (Garland Science, 2002).
40. Gaietta, G. et al. Multicolor and electron microscopic imaging of connexin trafficking. *Science* **296**, 503–507 (2002).
41. Dieterich, D. C. et al. In situ visualization and dynamics of newly synthesized proteins in rat hippocampal neurons. *Nat. Neurosci.* **13**, 897–905 (2010).
42. Wei, L. et al. Imaging complex protein metabolism in live organisms by stimulated Raman scattering microscopy with isotope labeling. *ACS Chem. Biol.* **10**, 901–908 (2015).
43. Lewis, C. A. et al. Tracing compartmentalized nadph metabolism in the cytosol and mitochondria of mammalian cells. *Mol. Cell* **55**, 253–263 (2014).
44. Liu, L. et al. Malic enzyme tracers reveal hypoxia-induced switch in adipocyte NADPH pathway usage. *Nat. Chem. Biol.* **12**, 345–352 (2016).
45. Kudryavtseva, M. V., Sakuta, G. A., Stein, G. I. & Kudryavtsev, BN. The metabolic zonation of glycogen synthesis in rat liver after fasting and refeeding. *Tissue Cell* **24**, 31–35 (1992).
46. Jungermann, K. & Katz, N. Functional specialization of different hepatocyte populations. *Physiol. Rev.* **69**, 708–764 (1989).
47. Fu, D. et al. In vivo metabolic fingerprinting of neutral lipids with hyperspectral stimulated Raman scattering microscopy. *J. Am. Chem. Soc.* **136**, 8820–8828 (2014).
48. Zhang, L. & Min, W. Bioorthogonal chemical imaging of metabolic changes during epithelial-mesenchymal transition of cancer cells by stimulated Raman scattering microscopy. *J. Biomed. Opt.* **22**, 1–7 (2017).
49. Hou, J., Williams, J., Botvinick, E., Potma, E. & Tromberg, B. J. Visualization of breast cancer metabolism using multimodal non-linear optical microscopy of cellular lipids and redox state. *Cancer Res.* **78**, 2503–2512 (2018).
50. Hong, W. et al. Antibiotic susceptibility determination within one cell cycle at single-bacterium level by stimulated Raman metabolic imaging. *Anal. Chem.* **90**, 3737–3743 (2018).
51. Saar, B. G. et al. Video-rate molecular imaging in vivo with stimulated Raman scattering. *Science* **330**, 1368–1370 (2010).
52. Saar, B. G., Johnston, R. S., Freudiger, C. W., Xie, X. S. & Seibel, E. J. Coherent Raman scanning fiber endoscopy. *Opt. Lett.* **36**, 2396 (2011).
53. Shen, Y., Xu, F., Wei, L., Hu, F. & Min, W. Live-cell quantitative imaging of proteome degradation by stimulated Raman scattering. *Angew. Chem. Int. Ed.* **53**, 5596–5599 (2014).
54. Wei, L. et al. Live-cell imaging of alkyne-tagged small biomolecules by stimulated Raman scattering. *Nat. Methods* **11**, 410–412 (2014).
55. Lu, F.-K. et al. Label-free DNA imaging in vivo with stimulated Raman scattering microscopy. *Proc. Natl Acad. Sci. USA* **112**, 11624–11629 (2015).

Acknowledgements

We thank F. Hu and C. Zheng for suggestions on this manuscript. W.M. acknowledges support from a National Institutes of Health Director's New Innovator Award (1DP2EB016573), NIH R01 (grant EB020892), the Alfred P. Sloan Foundation, the Camille and Henry Dreyfus Foundation and a Pilot and Feasibility grant from the New York Obesity Nutrition Research Center.

Author contributions

L.Z., L.S., Y.S. and W.M. designed the experiment. L.Z. and L.S. performed mouse labelling and imaging. L.Z., M.W., Y.L. and L.S. performed macromolecule isolation and analysis. Y.M. and N.Q. performed NMR measurement and analysis. L.Z., L.S., Y.S. and Y.M. analysed the data. Y. S., L.Z. and W.M. wrote the manuscript with contributions from all authors.

Competing interests

The authors declare no competing interests.

Additional information

Supplementary information is available for this paper at https://doi.org/10.1038/s41551-019-0393-4.

Reprints and permissions information is available at www.nature.com/reprints.

Correspondence and requests for materials should be addressed to W.M.

Publisher's note: Springer Nature remains neutral with regard to jurisdictional claims in published maps and institutional affiliations.

nature research

Corresponding author(s): Wei Min

Last updated by author(s): Feb 22, 2019

Reporting Summary

Nature Research wishes to improve the reproducibility of the work that we publish. This form provides structure for consistency and transparency in reporting. For further information on Nature Research policies, see Authors & Referees and the Editorial Policy Checklist.

Statistics

For all statistical analyses, confirm that the following items are present in the figure legend, table legend, main text, or Methods section.

n/a	Confirmed	
☒	☐	The exact sample size (*n*) for each experimental group/condition, given as a discrete number and unit of measurement
☒	☐	A statement on whether measurements were taken from distinct samples or whether the same sample was measured repeatedly
☒	☐	The statistical test(s) used AND whether they are one- or two-sided *Only common tests should be described solely by name; describe more complex techniques in the Methods section.*
☒	☐	A description of all covariates tested
☒	☐	A description of any assumptions or corrections, such as tests of normality and adjustment for multiple comparisons
☒	☐	A full description of the statistical parameters including central tendency (e.g. means) or other basic estimates (e.g. regression coefficient) AND variation (e.g. standard deviation) or associated estimates of uncertainty (e.g. confidence intervals)
☒	☐	For null hypothesis testing, the test statistic (e.g. *F*, *t*, *r*) with confidence intervals, effect sizes, degrees of freedom and *P* value noted *Give P values as exact values whenever suitable.*
☒	☐	For Bayesian analysis, information on the choice of priors and Markov chain Monte Carlo settings
☒	☐	For hierarchical and complex designs, identification of the appropriate level for tests and full reporting of outcomes
☒	☐	Estimates of effect sizes (e.g. Cohen's *d*, Pearson's *r*), indicating how they were calculated

Our web collection on statistics for biologists contains articles on many of the points above.

Software and code

Policy information about availability of computer code

Data collection	Images were collected with Olympus FluoView. Spectra were collected with LabSpec6.
Data analysis	ImageJ bundled with 64-bit Java 1.8.0_112 from https://imagej.nih.gov/ij/download.html, Origin and GraphPad were used for analysis.

For manuscripts utilizing custom algorithms or software that are central to the research but not yet described in published literature, software must be made available to editors/reviewers. We strongly encourage code deposition in a community repository (e.g. GitHub). See the Nature Research guidelines for submitting code & software for further information.

Data

Policy information about availability of data

All manuscripts must include a data availability statement. This statement should provide the following information, where applicable:

- Accession codes, unique identifiers, or web links for publicly available datasets
- A list of figures that have associated raw data
- A description of any restrictions on data availability

The authors declare that all data supporting the results in this study are available within the paper and its Supplementary Information. All raw and processed images generated in this work are available from the corresponding author on reasonable request.

Field-specific reporting

Please select the one below that is the best fit for your research. If you are not sure, read the appropriate sections before making your selection.

☒ Life sciences ☐ Behavioural & social sciences ☐ Ecological, evolutionary & environmental sciences

Life sciences study design

All studies must disclose on these points even when the disclosure is negative.

Sample size	A sample size of 3 was used in these qualitative studies.
Data exclusions	No data were excluded.
Replication	The results were reproducible.
Randomization	Newborn mice (postnatal 0–22 days old), and adult mice (3–5 months old) were separated into the two age groups.
Blinding	We designed the experiments to study newborn and adults mice, so it is not necessary to blind the group for this particular study.

Reporting for specific materials, systems and methods

We require information from authors about some types of materials, experimental systems and methods used in many studies. Here, indicate whether each material, system or method listed is relevant to your study. If you are not sure if a list item applies to your research, read the appropriate section before selecting a response.

Materials & experimental systems

n/a	Involved in the study
☒	☐ Antibodies
☐	☒ Eukaryotic cell lines
☒	☐ Palaeontology
☐	☒ Animals and other organisms
☒	☐ Human research participants
☒	☐ Clinical data

Methods

n/a	Involved in the study
☒	☐ ChIP-seq
☒	☐ Flow cytometry
☒	☐ MRI-based neuroimaging

Eukaryotic cell lines

Policy information about cell lines

Cell line source(s)	PC3, HeLa, MCF7, RWPE-1, U87MG, all obtained from ATCC.
Authentication	ATCC authenticated the cells.
Mycoplasma contamination	Cell lines tested negative for mycoplasma contamination.
Commonly misidentified lines (See ICLAC register)	No commonly misidentified cell lines were used.

Animals and other organisms

Policy information about studies involving animals; ARRIVE guidelines recommended for reporting animal research

Laboratory animals	Mice of strain C57BL/6J and strain J:NU were used in this study. Postnatal mice were 0–22 days old, and adult mice were 3–5 months old. All adult mice were female.
Wild animals	The study did not involve wild animals.
Field-collected samples	The study did not involve samples collected from the field.
Ethics oversight	All animal experiments were conducted in adherence to the experimental protocol approved by IACUC (AC-AAAQ0496).

Note that full information on the approval of the study protocol must also be provided in the manuscript.